Imparting high elastocaloric cooling potential to NiTi alloy by two-step enhancements

Junyu Chen [a,c], Chaoqun Zhao [a], Shubo Zhang [b], Wenjing Zhang [b], Wei Liu [b], Liping Lei [a], Upadrasta Ramamurty [c,d], Gang Fang [a,*]

[a] *State Key Laboratory of Clean and Efficient Turbomachinery Power Equipment, Department of Mechanical Engineering, Tsinghua University, Beijing 100084, China*

[b] *School of Materials Science and Engineering, Tsinghua University, Beijing 100084, China*

[c] *School of Mechanical and Aerospace Engineering, Nanyang Technological University, Singapore 639798, Republic of Singapore*

[d] *Institute of Materials Research and Engineering (IMRE), Agency for Science, Technology and Research (A*STAR), Singapore 138634, Republic of Singapore*

Abstract

The large adiabatic temperature change during the stress-induced phase transformation in the superelastic NiTi alloy makes it a leading candidate material for solid-state elastocaloric cooling applications. However, NiTi with a uniform grain structure generally offers either large cooling capacity or low energy dissipation, but not both. In an earlier study, we demonstrated that the alloy with graded grain sizes, obtained using differential annealing of heavily cold-worked sheets, can overcome this intrinsic limitation. However, non-transformable phases (residual martensite and amorphous phases), which are introduced into the microstructure during cold rolling, impair the full exploitation of the cooling potential of the graded NiTi. Here, we introduce an intermediate processing step, namely post-deformation annealing, which eliminates the undesirable phases while maintaining nanocrystallinity, before imparting

* The corresponding author.
E-mail address: fangg@tsinghua.edu.cn (G. Fang)

a microstructural gradient. Results show that the synergy between various microstructural elements results in a significant enhancement in the cooling capacity while keeping the energy dissipation low. Moreover, the functional fatigue performance of the graded alloy is also preferable to the conventional coarse-grained NiTi. The micromechanical reasons behind these improvements are elucidated by recourse to detailed experiments.

Keywords: Shape memory alloys; Functionally graded materials; Elastocaloric cooling; Mechanical incompatibility; Phase transformation

1. Introduction

Elastocaloric cooling, which exploits latent heat associated with the stress-induced solid-state phase transformation, is emerging as a promising green and more efficient alternative to the conventional vapor-compression technology [1, 2]. For it to be widely commercialized, however, solid refrigerant materials that simultaneously offer large cooling capacity and dissipate the least energy are the key [3]. Superelastic NiTi is a frontrunner among them, due to its considerable caloric capacity and outstanding mechanical properties [4-6]. A coarse-grained superelastic NiTi readily exhibits a large adiabatic temperature change (> 20 K) during loading or unloading, owing to the first-order martensitic transformation that it is susceptible to [7]. Its caloric capacity can be further enhanced by modulating the crystallographic compatibility between the parent (austenite) and product (martensite) phases [8]. However, a large hysteresis (i.e., energy dissipation) that accompanies the transformation cycle in the superelastic NiTi reduces its cooling efficiency significantly; it also accelerates the functional fatigue of the alloy [9-12]. The hysteretic dissipation could be minimized by refining the grain size through severe plastic deformation (SPD), which results in a second-order-like continuous transformation [13, 14]. This, however, occurs with a substantial compromise on the caloric capacity and ductility of the alloy [15, 16]. It follows that large cooling capacity and low hysteretic dissipation are generally mutually exclusive. Since the physical mechanisms responsible for these two competing properties are diagonally opposite [14, 17], typical strategies, such as chemical composition manipulation or microstructural fine tuning, are usually not viable for reconciling them [3]. Hence, the existing NiTi-

based elastocaloric materials with homogeneous microstructures are either designed for large cooling capacity or low energy dissipation, but not both [8, 14, 17, 18].

A similar 'conflict' between strength and ductility typically exists in most metallic materials [19]; one of the demonstrated ways to circumvent this problem is through the introduction of a steep grain-size gradient, which is often introduced through surface mechanical treatment (SMT) such as shot peening [20]. A similar strategy could also offer a solution for the trade-off between the large cooling capacity and the low dissipation of the superelastic NiTi, as demonstrated in the numerical simulation work [21, 22]. However, achieving a large grain-size gradient through SMT of a superelastic NiTi is difficult as its large damping capacity allows for the dissipation of the input kinetic energy through martensitic transformation, which results in a shallow plastic strain gradient [23, 24]. One way to circumvent this, which we demonstrated recently, is by varying the annealing with depth of a severely-deformed NiTi [9, 25]. Here, the high sensitivity of NiTi's microstructural evolution to the annealing temperature is exploited [26]. Results show that it is possible to balance low energy dissipation and large cooling capacity in NiTi by employing a graded microstructure [25]. In the severely-deformed microstructures (through cold rolling), however, non-transformable microstructural constituents, such as amorphous and martensite phases are present. Such phases prevent the full exploitation of the cooling potential of the graded NiTi [27]. It is difficult to remove them, while preserving low dissipation and high strength before introducing grain-size gradient, if the graded annealing process is employed directly. Since these constituents lead to sub-optimum properties, a suitable strategy is needed to eliminate

them. In addition, the effect of grain-size gradient on the elastocaloric cooling performance of the superelastic NiTi is not a well-understood phenomenon. The lack of quantitative information on the synergy between the heterogeneous microstructural domains that exist within the graded NiTi alloy is the reason behind this. While post-deformation annealing could eliminate the non-transformable components within the severely-deformed NiTi and enhance its cooling capacity [15, 28], both grain growth and dislocation density within the annealed NiTi need to be controlled carefully, as they would increase energy dissipation and reduce fatigue resistance [14]. In this context, the introduction of a post-deformation annealing step, which eliminates the undesirable phases and, in the process, optimizes the matrix for the subsequent laser surface annealing for generating gradient structure, would be ideal.

We pursue the above strategy in this work through nanocrystallization (prior to imparting a graded grain structure) of the cold-rolled sheets of superelastic NiTi. As a result, a combination of large cooling capacity and low dissipation and the resultant significant increase in cooling efficiency are achieved. The dual contributions of matrix enhancement and synergetic effect, which are responsible for the exceptional cooling performance, are elucidated and quantified.

2. Materials and experiments

2.1. Material preparation

The 1.52-mm-thick commercially obtained polycrystalline NiTi (Ti-50.8 at.% Ni) sheets employed in this study were first homogenized at 1073 K for one hour and then

repeatedly cold-rolled to a final thickness of 0.95 mm. They were then subjected to a post-deformation annealing at 573 K for 20 min and ice water quenched. Subsequently, the NiTi sheets were polished to mirror-like surfaces to remove mechanically-damaged and oxide surface layers and then subjected to laser surface annealing on the upper and lower surfaces to generate gradient microstructures. Tensile samples with a gauge size of 20 (length) × 3 (width) × 0.9 (thickness) mm^3 were wire-cut from the prepared NiTi sheets.

2.2. Experimental methods

Laser surface annealing of the post-deformation annealed (PDA) NiTi was performed on a Renishaw AM250 machine equipped with a 200 W Yb:YAG fiber laser with a spot diameter of 75 μm in a protective argon atmosphere. After several iterations, the following optimum parameter combination was selected: laser power of 100 W, scanning speed of 1000 mm s^{-1} and hatch spacing of 35 μm. Transmission electron microscope (TEM, JEM-2100F) and X-ray diffraction (XRD, Bruker-D8) were used to characterize microstructures. TEM foils from the predetermined depths were prepared by mechanically polishing away the redundant layers and then thinning by twin-jet electro-polishing in an electrolyte solution of 75 vol.% CH_3OH and 25 vol.% HNO_3 at a voltage of 20 V and a temperature of 245 K. XRD was performed over $35° < 2\theta < 50°$ at room temperature (~ 300 K), and the martensite (B19′) diffraction planes were indexed according to the following lattice parameters: $a = 2.889$ Å, $b = 4.120$ Å, $c = 4.622$ Å and $\beta = 96.8°$. Dislocation density is estimated using the high-resolution TEM images and by employing the Williamson-Hall method for the XRD data. The

volume fraction of the amorphous phase in the cold rolled samples was estimated through crystallization enthalpy measured by differential scanning calorimetry (DSC, TA Q2000) performed with a heating rate of 50 K min^{-1}.

Quasi-static tensile tests were performed under a nominal strain rate of 1×10^{-4} s^{-1}. The cooling potential assessment in a specific thermodynamic cycle was performed using a universal testing machine (Shimazu, AG-X). Strain and temperature fields were recorded using the digital image correlation technique (VIC-2D) and a high-frequency (200 Hz) infrared camera (FLIR, A615), respectively. To avoid the temperature measurement deviation caused by inhomogeneous phase transformation [9, 12, 14], the temperature change is determined by averaging the entire gauge section of the specimen. Stress and strain distributions across the specimen thickness were determined and analyzed by a commercial finite element software ABAQUS.

3. Results and discussion

3.1. Material fabrication and characterization

Figure 1 schematically illustrates the fabrication processes employed here for obtaining the superelastic NiTi with graded microstructure, which include cold rolling, post-deformation annealing, and finally laser surface annealing. The cold-rolled (CR) NiTi contains austenite (B2), residual martensite (B19′) and amorphous phases (Figs. 2a - h), consistent with prior observations [17, 29]. The crystalline phases contain a large number of nanodomains (~ 5 - 15 nm in size) that are separated by densely packed dislocation walls (Figs. 2a and c). The selected-area electron diffraction (SAED) pattern

shows split spots corresponding to the B2 and B19′ phases, and the diffuse rings indicate the amorphization of the matrix during the cold rolling (Fig. 2b). High-resolution transmission electron microscope (TEM) and the corresponding fast Fourier transform (FFT) images further confirm the presence of the amorphous structure with hallo-like reflection and the B2 and B19′ crystals with regular satellite spots (Figs. 2d - h). The residual B19′ and amorphous phases are stabilized by the high density of dislocations (~ 1.9×10^{16} m^{-2}) present in the microstructure. It is important to note that the residual B19′ and amorphous phases can no longer undergo stress-induced martensitic transformation and thereby lower the entropy change. To eliminate these non-transformable components, while retaining the low hysteretic dissipation of the nanocrystals, post-deformation annealing, which does not lead to both substantial dislocation annihilation and recrystallization, is performed. Bright- and dark-field TEM images and the sharp sole B2 diffraction ring in the SAED pattern suggest that the post-deformation annealed (PDA) NiTi consists of only B2 crystals with an average grain size of ~ 20 nm (Figs. 2i and j). The isolated $(110)_{B2}$ peak observed in the XRD patterns obtained under different *Chi* angles (Fig. 2k) and the near-linear heat-flow curve during heating (Fig. 2l) of the PDA NiTi further confirm that the residual B19′ and amorphous phases have almost completely transformed into B2 after annealing. Therefore, matrix optimization, which contains only nanocrystalline B2 (~ 20 nm) with high-density dislocations (5.2×10^{15} m^{-2}), is realized before introducing gradient structure, owing to the concurrent reverse transformation (B19′ to B2), crystallization of the amorphous phase, and partial recovery/recrystallization of the deformed grains.

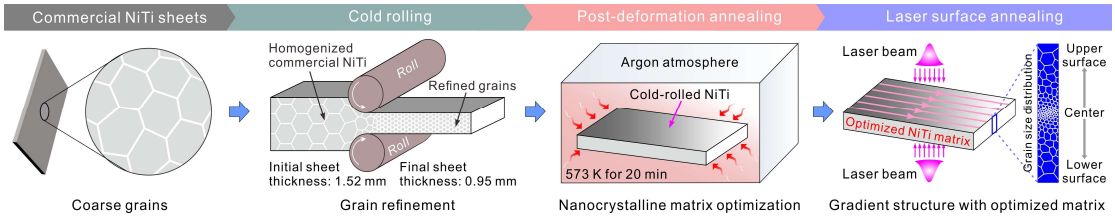

Fig. 1. Schematic illustrations of the manufacturing procedure utilized for obtaining the PDAGS NiTi.

The volume fraction of the amorphous phase of the CR NiTi is estimated to be 6.3% from the crystallization enthalpy (0.22 kJ mol^{-1}) of the exothermic peak of the heat-flow curve [15, 30]. Considering that B2 and B19′ account for ~ 51% and 49% of the crystal volume fraction, respectively, as estimated from the neutron diffraction data (Fig. S1), the volume fractions of B2 and B19′ phases in CR NiTi are determined to be ~ 47.79% and 45.92%, respectively. Thus, the amount of transformable B2 is approximatively increased by 109%, to almost 100% in PDA NiTi.

Layer surface annealing was further performed on PDA NiTi and the variations in the resultant microstructures with corresponding SAED patterns along the depth are shown in Fig. 2. More detailed microstructural features are provided in Fig. S2. The top 10-μm-deep layer features nearly equiaxed grains (with an average 603 nm diameter) with homogeneous intragranular contrast, clear and straight grain boundaries, and strain-free lattice structure (as evidenced by the SAED patterns), resulting from recrystallization and grain growth. As the depth increases to ~ 30 μm, the mean grain size reduces to 310 nm and the predominant wrinkle-like microstructural morphology with identifiable but curved grain boundaries and non-uniform contrast emerges. Upon going deeper, an increased number of fragmented grains with indistinguishable boundaries and complex strain contrast are observed. Consequently, the mean grain size

decreases to 123, 61 and 30 nm at the depths of ~ 75, 150 and 300 μm, respectively, and the corresponding SAED patterns gradually vary from arched spots to near-continuous rings. The central domain with an average grain size of ~ 20 nm exhibits no identifiable microstructural change compared with the PDA matrix (Figs. 2i and j), indicating negligible heat penetration from the laser source. The graded microstructures with B2 diffraction patterns alone (referred to as PDAGS NiTi hereafter) demonstrate that a continuous change in grain sizes spanning over thirty times is generated in the austenitic NiTi without introducing any undesirable phases.

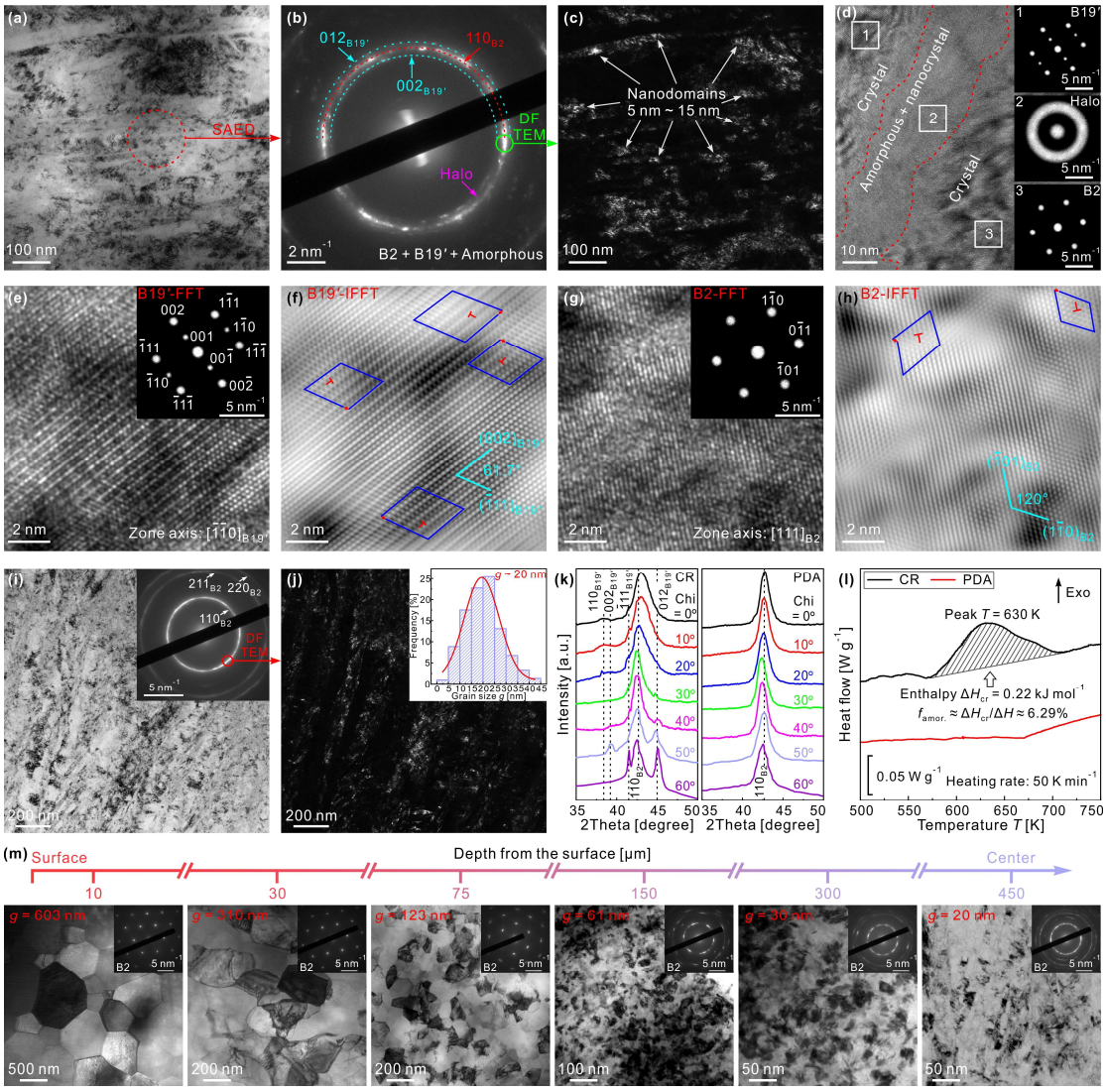

Fig. 2. Results of the characterization of CR, PDA and PDAGS NiTi. (a) - (h) Microstructures of CR NiTi. (a) The bright-field TEM image, (b) the SAED pattern and (c) the dark-field TEM micrograph. (d) High-resolution TEM and FFT images (the three insets) demonstrate the coexistence of amorphous, austenite (B2) and martensite (B19′) phases in CR NiTi. High-resolution TEM and inverse fast Fourier transform (IFFT) images of (e) - (f) B19′ and (g) - (h) B2 phases. Dislocations are identified with "T" symbols. (i) Bright-field and (j) dark-field TEM micrographs of PDA NiTi. The insets in (i) and (j) show the SAED pattern and the statistical grain size distribution, respectively. The results of (k) XRD and (l) DSC indicate that amorphous and B19′ phases were introduced during cold rolling but completely transformed back to B2 in PDA NiTi. ΔH_{cr} (= 0.22 kJ mol^{-1}) and ΔH (= 3.5 kJ mol^{-1}) are the crystallization enthalpy of CR and completely amorphous NiTi [30], respectively. (m) Bright-field TEM micrographs with SAED patterns at different depths of PDAGS NiTi.

3.2. Post-deformation annealing

A comparison of cooling performances between CR and PDA NiTi is conducted under (nominally) isothermal loading (1×10^{-4} s^{-1}) to pre-designated maximum tensile

strains (ε_{max} = 1% - 5%) and then rapid unloading (0.1 s^{-1}) (Fig. 3). The reverse phase transformation process during unloading can be considered adiabatic, since the total deformation time (within 0.5 s) is far less than the heat transfer time t_h (= 12 s, Fig. S3). Figure 3a presents the tensile stress-strain responses obtained with different maximum strains. CR NiTi first shows a quasi-linear response (ε < 3.5%) and then fails (ε = 5%) soon after yielding. In contrast, PDA NiTi exhibits good superelasticity throughout the ε_{max} range examined. For CR NiTi, the early superelastic behavior is a combined result of the hysteretic martensitic transformation of crystalline B2 and the elastic deformation of residual B19′ and amorphous phases [29]. Subsequent premature yielding (ε = ~ 4%) and failure (ε = ~ 5%) are caused by its inability to accommodate significant strain, which is a result of the small grain size and the near-saturated dislocation density within it [31]. In contrast, PDA NiTi shows a higher mechanical stability with negligible irrecoverable deformation (Fig. 3b). Owing to the increasing deformation irreversibility and phase transformation with ε_{max}, the energy dissipation ΔW (i.e., the hysteresis loop area in the stress-strain curves as defined in Fig. 3a) of both NiTi increases exponentially (Fig. 3c). ΔW of PDA NiTi rises slightly above that of CR one at low applied strain (ε_{max} < 3.5%), while a substantial reversal with a 60% decrease in ΔW appears with further deformation (ε_{max} = 4.5%). This result implies that reducing energy dissipation of metallic refrigerants only by grain refinement through SPD is not necessarily feasible and sometimes even counterproductive, due to the brittleness that SPD imparts to the alloy [32].

The adiabatic temperature drop $|\Delta T_{ad}|$ upon stress removal, a direct measure of

the cooling capacity of the material, increases monotonically with the applied strain, because of the increasing degree of phase transformation in both NiTi as shown in Fig. 3d. Notably, $|\Delta T_{ad}|$ of PDA NiTi is always larger than that of CR NiTi; for ε_{max} >3%, it is enhanced by 116% (inset in Fig. 3d) owing to the increased amount of the transformable B2 after matrix optimization. Besides, the reductions in the overall grain boundary area (by virtue of larger average grain size), dislocation density, and vacancies due to annealing also contribute to the observed improvement in the cooling capacity [14, 26].

To further compare the elastocaloric effect of both NiTi, the material's coefficient of performance (COP_{mat}), which is defined as the amount of cooling produced per unit dissipated work, is evaluated. COP_{mat} shows an inverse dependence on ε_{max} (Fig. 3e), since ΔW increases faster than $|\Delta T_{ad}|$ with ε_{max}. COP_{mat} of PDA NiTi is higher than that of CR NiTi under different ε_{max}, with a maximum enhancement of 435% at ε_{max} = 4.5% (inset in Fig. 3e). These results unequivocally confirm that a substantial enhancement in the elastocaloric performance of the nanocrystalline NiTi can be realized through matrix optimization.

Physically, post-deformation annealing not only stabilizes the martensitic transformation due to grain refinement (~ 20 nm) and the presence of high-density dislocations (5.2×10^{15} m^{-2}) to reduce dissipation, but also eliminates the non-transformable components via crystallization and partial recovery/recrystallization to increase cooling capacity. Accordingly, a favorable reconciliation between low dissipation and large refrigeration capacity, and the consequent high cooling efficiency

are preliminarily achieved. Nevertheless, as stress-induced phase transformation is partially suppressed by the limited accommodation capability of martensite due to the small grain sizes (~ 20 nm) of PDA NiTi [33], imparting a gradient grain structure to it could further enhance its elastocaloric cooling potential.

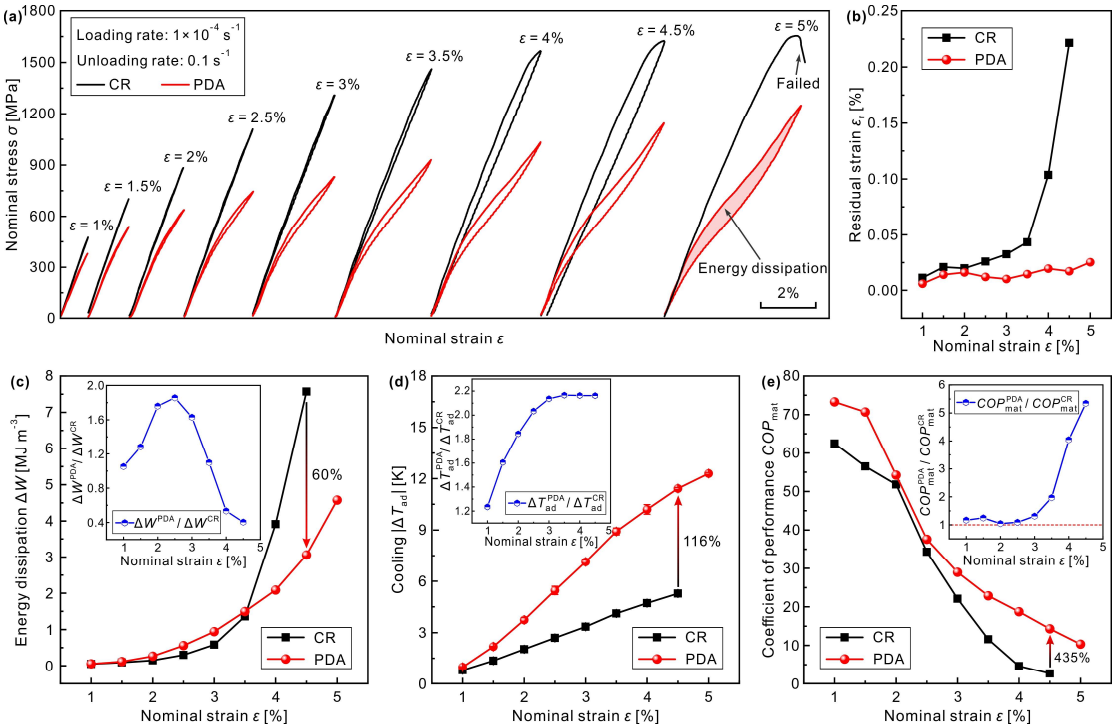

Fig. 3. A comparison of elastocaloric cooling performances between the cold-rolled (CR) and the post-deformation annealed (PDA) NiTi. (a) Strain-dependent stress-strain curves upon isothermal loading and adiabatic unloading and (b) the resultant residual strain after unloading. (c) energy dissipation ΔW, (d) cooling temperature drop $|\Delta T_{ad}|$ and (e) coefficient of performance COP_{mat} of CR and PDA NiTi under different strains. The insets in (c) - (e) show the corresponding performance ratios.

3.3. Evaluation of the cooling potential of the PDAGS NiTi

Figure 4 compares the thermomechanical properties of various types of NiTi examined in this study, in which PDA and GS NiTi represent the freestanding specimens that are fabricated only by post-deformation annealing and laser surface treatment on the CR substrate, respectively. PDAGS NiTi exhibits a mild 'strain-

hardening' type martensitic transformation (Fig. 4a), which is distinct from the near-linear response in CR and PDA NiTi and the steep curve of GS NiTi [25], and the plateau-type superelasticity in the coarse-grained (CG) NiTi (with an average grain size of 1500 nm; Fig. S4). Results of the elastocaloric studies on the five NiTi alloys indicate that PDAGS NiTi combines a large $|\Delta T_{ad}|$ with low ΔW (Fig. 4b), which contrasts sharply with the strong trade-off between $|\Delta T_{ad}|$ and ΔW of CR and CG NiTi. Apart from the 261% enhancement in $|\Delta T_{ad}|$ and 77% reduction in ΔW relative to CR and CG NiTi, respectively, enhancements of 69% and 49% improvements in the cooling capacity of PDAGS NiTi, compared with PDA and GS NiTi respectively, are realized. Furthermore, PDAGS NiTi exhibits a larger cooling capacity and dissipates less than a quarter of the energy relative to CG NiTi, which obviously cannot be afforded by either the optimized matrix or the gradient structure alone.

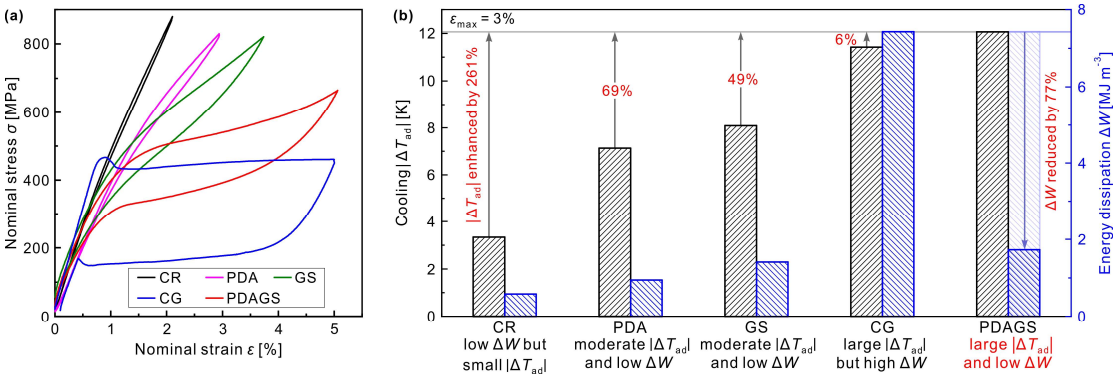

Fig. 4. Thermomechanical properties of CR, PDA, GS, CG and PDAGS NiTi. (a) Quasi-static tensile stress-strain curves. (b) Preliminary results of cooling $|\Delta T_{ad}|$ and energy dissipation ΔW under an applied strain of 3%.

A detailed comparison of the elastocaloric cooling performances of PDAGS and a commercially available CG NiTi is carried out with ε_{max} ranging from 1% to 6% (with an interval of 0.5% as shown in Fig. 5a). Due to the large stress hysteresis and the

apparent irrecoverable deformation (inset in Fig. 5b), ΔW of CG NiTi is 1.5 ~ 9 times that of PDAGS NiTi (Fig. 5b). It is seen that altering the avalanche-like phase transformation to a continuous one is effective in decreasing ΔW. As expected, $|\Delta T_{ad}|$ increases with ε_{max} in both PDAGS and CG NiTi (Fig. 5c). However, $|\Delta T_{ad}|$ of PDAGS NiTi exceeds that of CG NiTi when $\varepsilon_{max} > 3\%$ (inset in Fig. 5c), and the underlying mechanisms are discussed in the next section. Specifically, the PDAGS NiTi refrigerant can possess a comparable and even higher $|\Delta T_{ad}|$ yet reduce ΔW by 51% - 86% (Fig. S5) compared with CG NiTi, which gives rise to a multifold increase (up to 483%) in COP_{mat} (Fig. 5d).

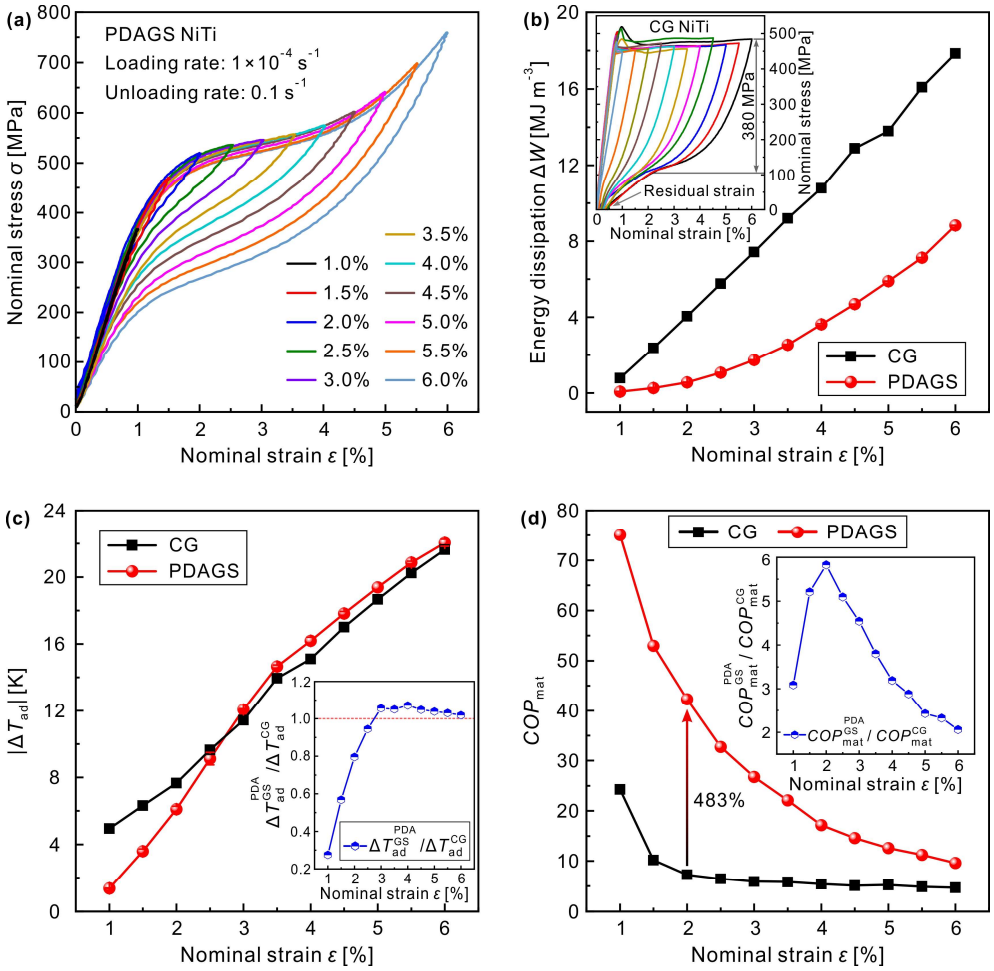

Fig. 5. A comparison of elastocaloric cooling performances between PDAGS and typical CG NiTi. (a) Stress-strain curves of PDAGS NiTi upon isothermal loading and adiabatic unloading. (b) ΔW, (c) $|\Delta T_{ad}|$ and (d) COP_{mat} of PDAGS and CG NiTi under different strains. The inset in (b) depicts the stress-strain curves of CG NiTi. Insets in (c) and (d) exhibit the corresponding performance ratios.

Next, we evaluate the functional stability of the mechanical and elastocaloric properties of PDAGS NiTi. Figure 6 shows the evolution of the stress-strain curves and the elastocaloric effect of PDAGS and CG NiTi under cyclic tensile loading. CG NiTi displays inferior superelastic reversibility as the residual strain accumulates rapidly to 1.1% only after 10 tensile cycles (Fig. 6a). Such an accumulation of irrecoverable deformation decreases the volume fraction of the transformable austenite and hinders the subsequent martensitic transformation [34-36]. Correspondingly, $|\Delta T_{ad}|$ decreases by as much as 46% from 14.66 K in the first cycle to 7.95 K in the 10th cycle (Fig. 6b).

In comparison, no pronounced degradation in both superelasticity and elastocaloric effect is observed up to 100 cycles in PDAGS NiTi. It is known that the irrecoverable deformation of NiTi upon multi-superelastic cycling is essentially linked to the crystallographic incompatibility between the austenitic and martensitic phases during transformation [14, 34], with a higher mismatch facilitating more dislocation slip. This understanding leads to infer that the observed functional stability of PDAGS NiTi stems from the uniform and continuous martensitic transformation with spatially homogeneous strain distribution (Fig. 7a); the typical occurrence of transformation-induced dislocations at the austenite-martensite interfaces is largely suppressed due to the absence of sharp Lüders bands [37]. It is reasonable to assume that martensite simultaneously nucleates and grows at many sites in PDAGS NiTi through the mutual accommodation between fine and coarse grains. Once the Lüders-like deformation in its coarse-grained surface layers is suppressed by the nanocrystalline core effectively, an overall uniform transformation occurs as shown in Fig. 7a. The uniform and stabilized transformation in PDAGS NiTi is also confirmed by the near-identical hardening stress-strain curves of the local and average mechanical responses (Fig. 7b), which are in contrast with the inhomogeneous deformation behavior with evident strain concentration in CG NiTi. In addition, the improved strength of PDAGS NiTi relative to that of CG NiTi would also elevate the resistance against the plastic deformation from localized yielding and thus contribute to long-term mechanical stability [38]. Notice that the uniform deformation reduces the intrinsic dissipation from interfacial friction at the moving phase boundaries between transforming phases and accounts for

the low ΔW achieved in PDAGS NiTi (Fig. 5b). Consequently, in contrast to the commercial CG NiTi, PDAGS NiTi not only markedly reduces ΔW but also increases $|\Delta T_{ad}|$, resulting in high cooling efficiency and preferable functional fatigue resistance.

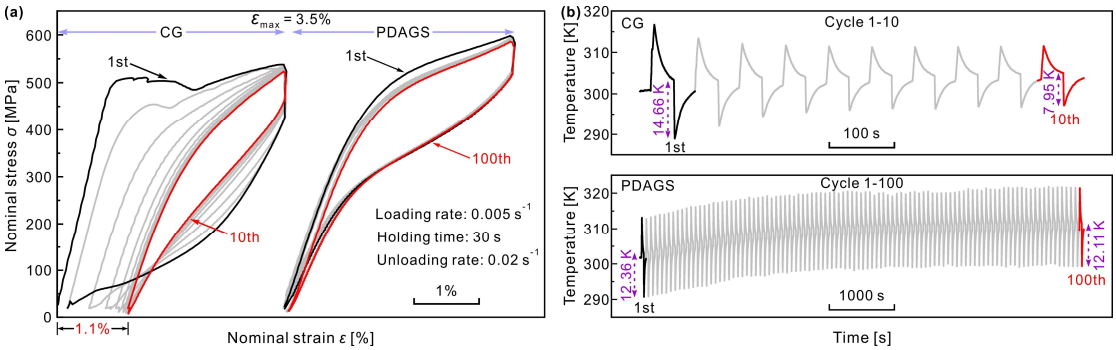

Fig. 6. Functional stability of (a) the mechanical response and (b) the elastocaloric effect of PDAGS and CG NiTi under cyclic tension.

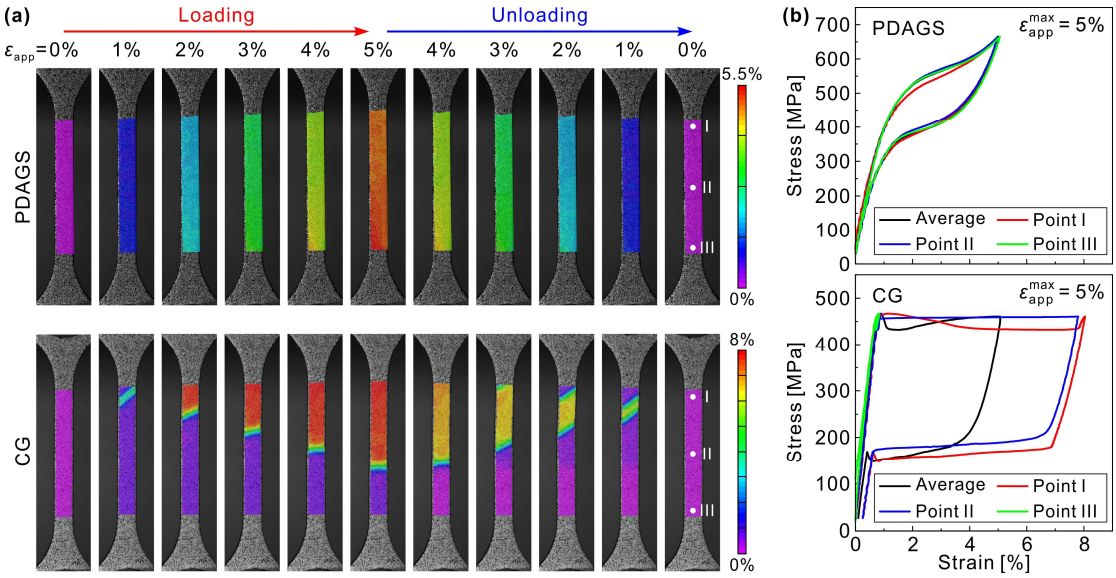

Fig. 7. Characteristics of martensitic transformation of PDAGS and CG NiTi upon loading and unloading. (a) Representative full-field strain patterns and (b) the local stress-strain curves recorded at different positions marked on (a) compared with the globally average mechanical response.

To further evaluate the refrigeration potential of PDAGS NiTi, we compare its cooling performance with that of other solid-state caloric material candidates. The PDAGS NiTi refrigerant stands out in terms of COP_{mat} along with a favorable

combination of large $|\Delta T_{ad}|$ and low ΔW, compared to common CR and CG NiTi (Fig. 8a). $|\Delta T_{ad}|$ of PDAGS NiTi is roughly fourfold and double that of the CR and CG NiTi, respectively, under near equal dissipated work ΔW (inset in Fig. 8a). Figure 8b presents $|\Delta T_{ad}|$ as a function of the grain size of the conventional NiTi with different microstructures (heat treatment conditions provided in Table S1), in which $|\Delta T_{ad}|$ rapidly increases with grain size before saturation. The corresponding mechanical behavior gradually changes from a quasi-linear stress-strain response in the alloy with 12-nm grain size to the typical plateau-type superelasticity in the 1500-nm one (inset in Fig. 8b). PDAGS NiTi exhibits a larger $|\Delta T_{ad}|$ than the freestanding counterparts regardless of grain sizes, including that with grain size (~ 603 nm) similar to that of its topmost layer (i.e., the most powerful microstructural component in terms of the grain size).

Figure 8c compares $|\Delta T_{ad}|$ versus ΔW data of the materials examined in this work and those reported in the literature [9, 10, 18, 25, 39-64]. It shows that the cooling performance of PDAGS NiTi surpasses that of the common CR and CG NiTi, and the alone PDA and GS ones. Its location on the upper left of the $|\Delta T_{ad}|$ - ΔW space represents a greater synergy between large cooling capacity and low dissipation than most elastocaloric refrigerant candidates (inset in Fig. 8c). It should be noted that larger $|\Delta T_{ad}|$ (> 30 K) of elastocaloric materials exists outside the $|\Delta T_{ad}|$ - ΔW space but at the expense of substantially increased ΔW and reduced durability [8, 65, 66]. More importantly, PDAGS NiTi improves COP_{mat} by 75%, 80% and 410% compared to PDA, GS and CG NiTi, respectively, under the same $|\Delta T_{ad}|$ of ~ 10 K (inset in Fig. 8d),

which makes it more efficient than the crowded solid caloric materials (Fig. 8d).

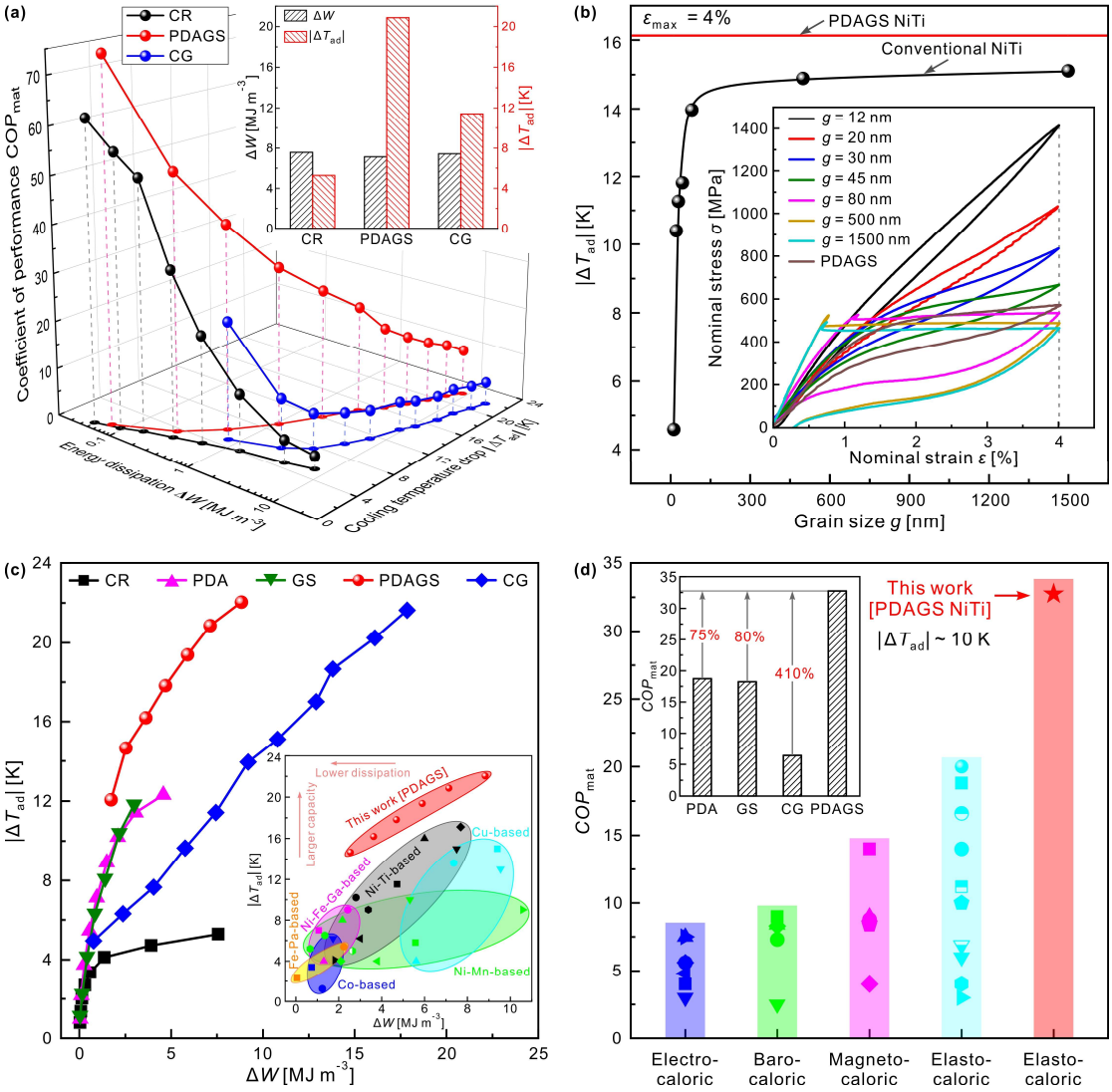

Fig. 8. A comparison of cooling performances between PDAGS NiTi and other caloric materials. (a) A summary of $|\Delta T_{ad}|$, ΔW and COP_{mat} of PDAGS NiTi and the typical CR and CG counterparts. The inset compares their cooling capacity $|\Delta T_{ad}|$ under equal dissipated work ΔW. (b) A comparison of $|\Delta T_{ad}|$ between PDAGS NiTi and the regular NiTi with various grain sizes at ε_{max}= 4%. The inset shows the corresponding mechanical responses. (c) $|\Delta T_{ad}|$ versus ΔW for PDAGS NiTi, CR, PDA, GS and CG counterparts and reported elastocaloric materials [9, 10, 18, 25, 39-64]. (d) Energy efficiency COP_{mat} of the PDAGS NiTi in comparison with that of PDA, GS and CG counterparts, electrocaloric [67-70], barocaloric [71-73] magnetocaloric [67, 74-76] and elastocaloric [2, 5, 7, 44, 54, 77, 78] refrigerants under an almost comparable cooling capacity ($|\Delta T_{ad}|$ ~ 10 K).

3.4. Synergetic effect for elastocaloric cooling

To elucidate that the cooling potential of PDAGS NiTi surpasses that of the

freestanding PDA NiTi and other aforementioned counterparts, we quantified another physical mechanism (i.e., synergetic effect) besides the matrix enhancement by combining experiment and simulation. Since the gradation in the microstructure occurs laterally across the thickness of PDAGS NiTi (Fig. 2m), the temperature change of the lateral surface during a Brayton-like cycle is monitored. It is shown that the different constituent domains along the thickness contain diverse microstructures (with grain sizes ranging from 20 to 603 nm) yet show a rather consistent elastocaloric effect (Fig. 9a), demonstrating a pronounced synergetic effect between heterogeneous layers.

Next, we examine the influence of gradient structure on the thermomechanical behavior of PDAGS NiTi. For this purpose, we approximate it as an integrated sum of numerous thin layers with gradually varying microstructures and mechanical properties [25, 79]. It is found that the tensile stress-strain responses (Fig. 9b) and the corresponding cooling temperature drops (Fig. 9c) change noticeably as the surface gradient layers are progressively removed from both laser-treated sides of the PDAGS specimen. The mechanical behavior gradually 'stiffens' as the surface layers are removed (Fig. 9b). Correspondingly, martensitic transformation becomes more and more difficult as evidenced by the elevated transformation stress, steeper hardening responses, and reduced hysteresis loop, due to the increase of volume fractions of grain boundaries (Fig. 2m). As a result, the enhancement in the cooling capacity imparted by the heterogeneous layers becomes weaker and eventually disappears (Fig. 9c). Specifically, ΔT_{ad} decreases from an initial -16.36 K to the final -11.34 K, indicating that the cooling capacity is almost retrogressed to that of the PDA nanocrystalline

matrix (ΔT_{ad} = -10.2 K, Fig. 3d) after largely removing the surface gradient layers (~290 μm). These findings suggest that the gradient structure enhances the elastocaloric cooling performance through synergetic interaction between different layers with varying grain sizes.

The synergetic enhancement is quantified by slicing the integrated PDAGS NiTi specimen into three thin layers (i.e., two 300-μm thick CG layers and a 300-μm thick core, inset in Fig. 9d). $|\Delta T_{ad}|$ of the original PDAGS NiTi with full thickness (red curve) is comparable to or slightly higher than that of its individual CG constituent layers (blue curve) and substantially exceeds that of the core (black curve) as shown in Fig. 9d. The synergetic enhancement in the cooling capacity of PDAGS NiTi is quantified by the volume fraction-based rule of mixtures (ROM) [80]:

$$\Delta T_{ad}^{ROM} = V_{CG\ layer}\Delta T_{ad}^{CG\ layer} + V_{Core}\Delta T_{ad}^{Core} \quad (1)$$

where $\Delta T_{ad}^{CG\ layer}$ and ΔT_{ad}^{Core} are the adiabatic temperature drops of the freestanding CG layer and the core, respectively. $V_{CG\ layer}$ and V_{Core} represent their volume fractions which are identical to the cross-sectional area fractions. The predicted $|\Delta T_{ad}|$ (green curve) by ROM is much lower than the experimental result (red curve) as shown in Fig. 9d. This is because the interlayer interaction in PDAGS NiTi was neglected in ROM. The extra enhancement in cooling capacity is further visualized by the light pink shadow region (Fig. 9d), and an additional improvement as high as 15% is achieved when $\varepsilon_{max} > 3\%$ (Fig. S6). It should be noted that the slice method to calculate the synergetic enhancement effect is accurate, in principle, if we can peel off all homogeneous components from the integrated PDAGS specimen to individually

measure their cooling performances. However, it is experimentally difficult or impossible due to the requirement of a specific specimen size during tensile testing. Therefore, the synergetic enhancement, estimated using the difference between the measured $|\Delta T_{ad}|$ and the predicted value using ROM based on the three constituent layers, is likely to be a significant underestimate.

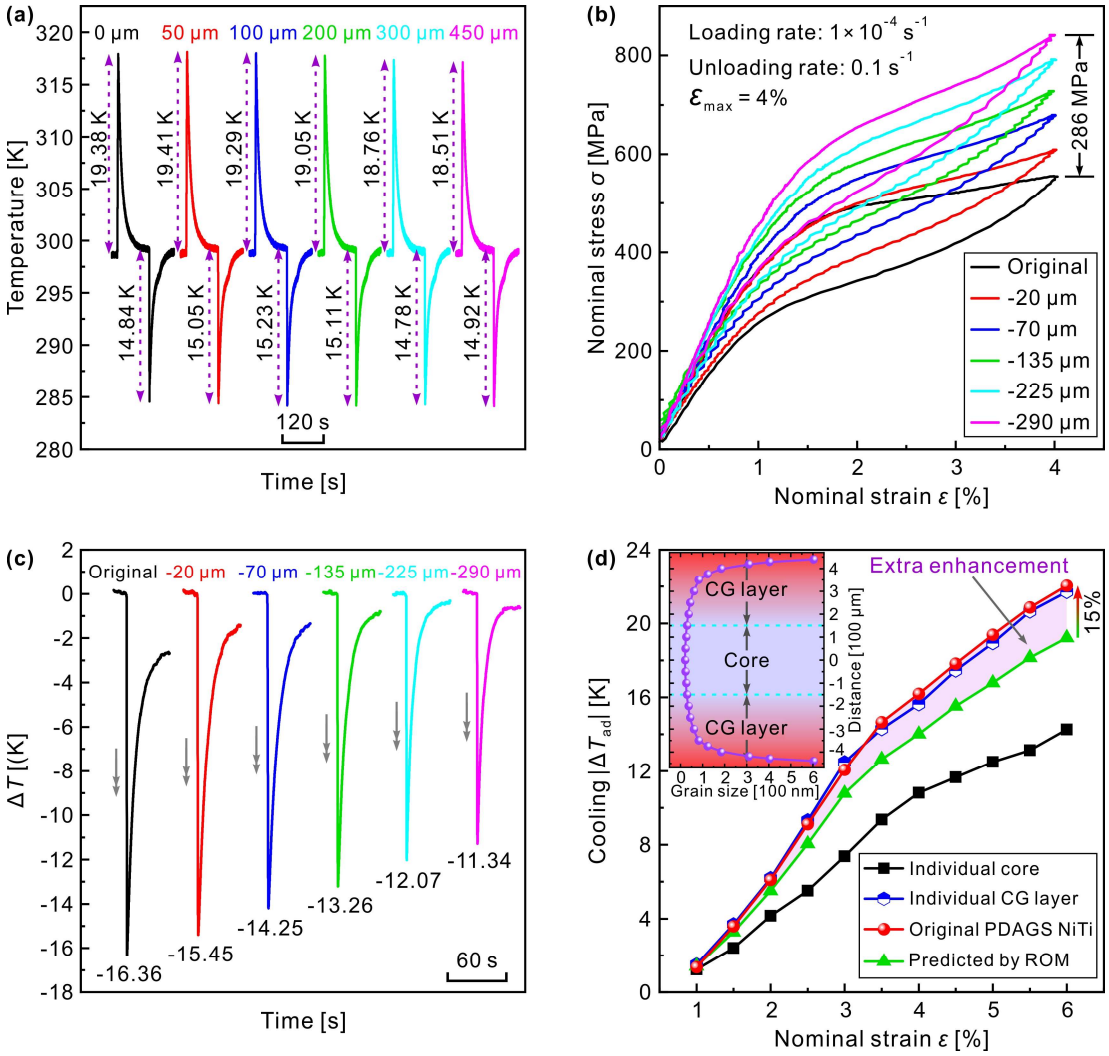

Fig. 9. Synergetic effect in PDAGS NiTi for the improved elastocaloric properties. (a) Time-dependent temperature evolution of the constituent layers at different depths. (b) Tensile stress-strain curves and (c) the corresponding cooling temperature drop changing with surface layers removed from both laser-treated sides of the PDAGS specimen. The legend denotes the layer thickness reduction from both surfaces. (d) Strain-dependent cooling $|\Delta T_{ad}|$ of the original PDAGS specimen, the constituent CG surface layers and nanocrystalline core, and the predicted value using the rule of mixture (ROM). The light pink shadow region shows the extra enhancement. The inset illustrates the grain size distribution and the rough domain division along the depth.

To probe the origin of the synergy observed in PDAGS NiTi, we investigated the stress and strain distributions across the thickness using a commercial finite element software, ABAQUS. Considering the symmetry of the specimen, one-eighth of the gauge section of the tensile specimen was simulated; its dimensions, meshes and boundary conditions are shown in Fig. 10a. The constitutive relationships for the eight separate layers with different grain sizes were obtained from experimental uniaxial tensile stress-strain responses measured (Fig. S7). Figures 10b and c show the simulation results at a tensile strain of 5% in the *z*-direction (tensile direction). A large stress difference ($\Delta\sigma_z$ = 678 MPa) with stress gradient up to 1.5 MPa/μm is observed (Fig. 10b), due to the mechanical incompatibility among diverse layers with considerable microstructural heterogeneity (Fig. 2m). The grain-size gradient also induces a macroscopic lateral strain difference ($\Delta\varepsilon_x$ = 0.37%), in which the softer surface CG layers shrink more than the harder central core (Fig. 10c). When the shrinking CG layers are constrained by the core, a lateral tensile stress develops [79]. Since no external stress is applied laterally in the *x*-direction, a lateral compressive stress has to be generated in the core to balance the tensile stress in the CG layers. As a result, σ_x, which should be zero in homogeneous materials, is positive in the soft CG layer and negative in the hard core (Fig. 10b), and the applied uniaxial stress is converted to a complex biaxial stress state (inset in Fig. 10b). The re-distribution of stress and strain enables the synergetic enhancement between heterogeneous layers. Physically, the nanocrystalline core carries more load ($\Delta\sigma_z$ = 678 MPa, Fig. 10b) and homogenizes global martensitic transformation (i.e., strain delocalization, Fig. 7a) for

low dissipation (Fig. 5b) and enhanced repeatability (Fig. 6). On the other hand, the CG surface layers accommodate more deformation (Fig. 10c) for strong caloric effect [22]. In addition, the pronounced superelastic deformation difference together with multiaxial stresses is accommodated by generating extra martensite variants to fulfill strain continuity [81], which might further enhance the refrigeration performances [8, 22]. Such synergetic effect activated under superelasticity represents a novel mechanism exploiting the principles of both materials science and mechanics for the improvement of elastocaloric properties. It should be noted that the employed model is a simplified one. However, it can qualitatively describe the mechanical incompatibility of PDAGS NiTi under loading. More detailed numerical simulation results concerning thermomechanical properties of graded NiTi can be found in our recent work [22].

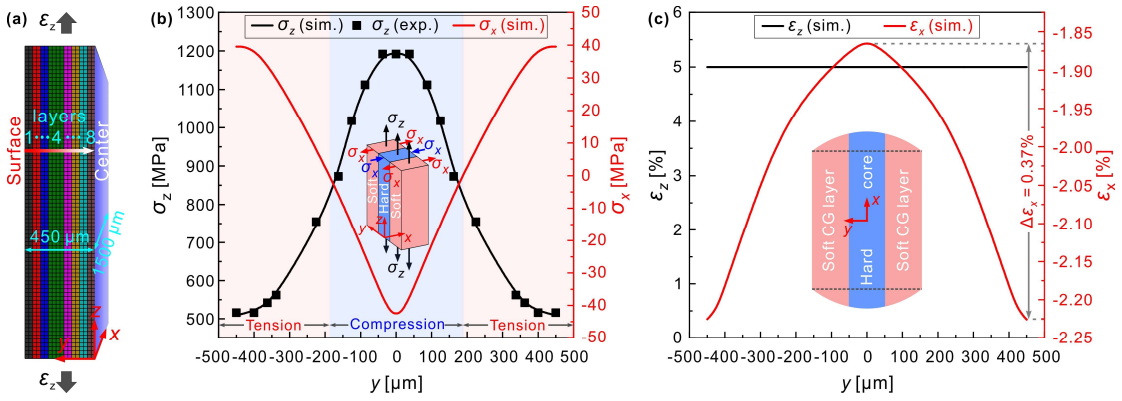

Fig. 10. Stress state change and strain re-distribution across the thickness of PDAGS NiTi under ε_z = 5%. (a) Schematic finite element model showing one-eighth of the gauge section of the specimen subjected to uniaxial external tension along the *z*-direction. The origin of the coordinates locates at the specimen's geometric center. (b) Stress σ_z and σ_x and (c) strain ε_z and ε_x distributing along the *y*-axis (i.e., the depth direction with microstructural gradient). The insets in (b) and (c) illustrate the stress state and the lateral strain gradient, respectively.

4. Conclusion

In summary, we achieve a favorable synergy between large cooling capacity and low energy dissipation in PDAGS NiTi refrigerant by post-deformation annealing to optimize matrix and subsequent laser surface annealing to introduce grain-size gradient microstructure. The developed PDAGS NiTi shows a larger adiabatic temperature change relative to conventional coarse-grained NiTi while dissipates much less energy, and thereby leading to a multifold increase in cooling efficiency, which makes it preferable to its freestanding matrix and gradient-structured constituents. The enhanced cooling performances of PDAGS NiTi are mainly attributable to the dual mechanisms of matrix enhancement and synergetic effect, which are enabled by nanocrystalline matrix optimization and interlayer interaction of gradient structure, respectively. Specifically, matrix enhancement not only stabilizes transformation via grain refinement and dense dislocations to reduce dissipation, but also eliminates non-transformable residual martensite and amorphous phases to improve cooling capacity. Synergetic enhancement between heterogeneous domains is generated by interlayer mechanical incompatibility, where the finer grains carry more load and homogenize global transformation for low dissipation and the coarser grains offer more deformation for strong caloric effect. The work would guide future endeavours and innovations in developing high-performance refrigerants in a wide variety of ferroelastic materials for solid-state cooling.

Acknowledgments

This work was supported by the National Key Research and Development

Program of China (No. 2017YFB0701801). The work at Nanyang Technological University was supported by the Agency for Science, Technology and Research (A*STAR) of Singapore via the Structural Metal Alloys Programme (No. A18B1b0061). The authors acknowledge useful discussions with Huilong Hou from Beihang University.

Credit author statement

Junyu Chen: Conceptualization, Data curation, Investigation, Formal analysis, Writing - original draft. **Chaoqun Zhao**: Software. **Shubo Zhang**: Investigation, Methodology. **Wenjing Zhang**: Investigation, Methodology. **Wei Liu:** Software, Methodology. **Liping Lei**: Resources, Funding acquisition. **Upadrasta Ramamurty**: Supervision, Writing - review & editing. **Gang Fang**: Supervision, Writing - review & editing.

References

[1] W. Goetzler, R. Zogg, J. Young, C. Johnson, Energy savings potential and RD&D opportunities for non-vapor-compression HVAC technologies, USA: US Department of Energy, Office of Energy Efficiency and Renewable Energy, Building Technologies Office (2014).

[2] S. Qian, Y. Geng, Y. Wang, J. Ling, Y. Hwang, R. Radermacher, I. Takeuchi, J. Cui, A review of elastocaloric cooling: Materials, cycles and system integrations, Int. J. Refrig. 64 (2016) 1-19.

[3] J. Chen, L. Lei, G. Fang, Elastocaloric cooling of shape memory alloys: A review, Mater. Today Commun. 28 (2021) 102706.

[4] J. Cui, Y. Wu, J. Muehlbauer, Y. Hwang, R. Radermacher, S. Fackler, M. Wuttig, I. Takeuchi, Demonstration of high efficiency elastocaloric cooling with large ΔT using NiTi wires, Appl. Phys. Lett. 101(7) (2012) 073904.

[5] J. Chen, K. Zhang, Q. Kan, H. Yin, Q. Sun, Ultra-high fatigue life of NiTi cylinders for compression-based elastocaloric cooling, Appl. Phys. Lett. 115(9) (2019) 093902.

[6] Y. Zhang, C. Yu, D. Song, Y. Zhu, Q. Kan, G. Kang, Solid-state cooling with high elastocaloric strength and low driving force via NiTi shape memory alloy helical springs: Experiment and theoretical model, Mech. Mater. 178 (2023) 104575.

[7] L. Porenta, P. Kabirifar, A. Žerovnik, M. Čebron, B. Žužek, M. Dolenec, M. Brojan, J. Tušek, Thin-walled Ni-Ti tubes under compression: ideal candidates for efficient and fatigue-resistant

elastocaloric cooling, Appl. Mater. Today 20 (2020) 100712.
[8] D. Cong, W. Xiong, A. Planes, Y. Ren, L. Mañosa, P. Cao, Z. Nie, X. Sun, Z. Yang, X. Hong, Colossal elastocaloric effect in ferroelastic Ni-Mn-Ti alloys, Phys. Rev. Lett. 122(25) (2019) 255703.
[9] J. Chen, L. Xing, G. Fang, L. Lei, W. Liu, Improved elastocaloric cooling performance in gradient-structured NiTi alloy processed by localized laser surface annealing, Acta Mater. 208 (2021) 116741.
[10] C. Bechtold, C. Chluba, R. Lima de Miranda, E. Quandt, High cyclic stability of the elastocaloric effect in sputtered TiNiCu shape memory films, Appl. Phys. Lett. 101(9) (2012) 091903.
[11] Y. Zhang, G. Kang, H. Miao, C. Yu, Cyclic degeneration of elastocaloric effect for NiTi shape memory alloy: Experimental observation and constitutive model, Int. J. Solids Struct. 248 (2022) 111638.
[12] V.V. Shastry, G. Singh, U. Ramamurty, On the fatigue life enhancement due to periodic healing of a NiTi shape memory alloy, Mater. Sci. Eng. A 815 (2021) 141272.
[13] J. Chen, Y. Wu, H. Yin, In situ multi-field investigation of grain size effects on the rate-dependent thermomechanical responses of polycrystalline superelastic NiTi, Mater. Lett. 259 (2020) 126845.
[14] J. Chen, L. Lei, G. Fang, D. Wang, Achieving great comprehensive elastocaloric cooling performances of superelastic NiTi by grain size engineering, Mater. Today Nano 21 (2023) 100279.
[15] J. Chen, L. Lei, G. Fang, Grain-size effects on the temperature-dependent elastocaloric cooling performance of polycrystalline NiTi alloy, J. Alloys Compd. 927 (2022) 166951.
[16] Q. Liang, S. Zhao, C. Liang, T. Zhao, D. Wang, X. Ding, S. Li, Y. Wang, Y. Zheng, X. Ren, M. Mills, Y. Wang, Strain states and unique properties in cold-rolled TiNi shape memory alloys, Acta Mater. 231 (2022) 117890.
[17] H. Lin, P. Hua, Q. Sun, Effects of grain size and partial amorphization on elastocaloric cooling performance of nanostructured NiTi, Scr. Mater. 209 (2022) 114371.
[18] H. Hou, E. Simsek, T. Ma, N.S. Johnson, S. Qian, C. Cissé, D. Stasak, N. Al Hasan, L. Zhou, Y. Hwang, R. Radermacher, V.I. Levitas, M.J. Kramer, M.A. Zaeem, A.P. Stebner, R.T. Ott, J. Cui, I. Takeuchi, Fatigue-resistant high-performance elastocaloric materials made by additive manufacturing, Science 366(6469) (2019) 1116-1121.
[19] K. Lu, Making strong nanomaterials ductile with gradients, Science 345(6203) (2014) 1455-1456.
[20] T. Fang, W. Li, N. Tao, K. Lu, Revealing extraordinary intrinsic tensile plasticity in gradient nano-grained copper, Science 331(6024) (2011) 1587-1590.
[21] B. Xu, J. Xiong, C. Yu, C. Wang, Q. Wang, G. Kang, Improved elastocaloric effect of NiTi shape memory alloys via microstructure engineering: A phase field simulation, Int. J. Mech. Sci. 222 (2022) 107256.
[22] Q. Zhang, J. Chen, G. Fang, From mechanical behavior and elastocaloric effect to microscopic mechanisms of gradient-structured NiTi alloy: A phase-field study, Int. J. Plast. 171 (2023) 103809.
[23] J. Cai, S. Mao, Y. Liu, L. Cui, J. Zhang, Z. Zhang, X. Han, Nb/NiTi laminate composite with high pseudoelastic energy dissipation capacity, Mater. Today Nano 19 (2022) 100238.
[24] K. Yan, P. Wei, F. Ren, W. He, Q. Sun, Enhance fatigue resistance of nanocrystalline NiTi by laser shock peening, Shap. Mem. Superelasticity 5(4) (2019) 436-443.
[25] J. Chen, B. Liu, L. Xing, W. Liu, L. Lei, G. Fang, Toward tunable mechanical behavior and enhanced elastocaloric effect in NiTi alloy by gradient structure, Acta Mater. 226 (2022) 117609.
[26] A. Ahadi, Q. Sun, Stress hysteresis and temperature dependence of phase transition stress in nanostructured NiTi—Effects of grain size, Appl. Phys. Lett. 103(2) (2013) 021902.
[27] P. Wei, P. Hua, M. Xia, K. Yan, H. Lin, S. Yi, J. Lu, F. Ren, Q. Sun, Bending fatigue life enhancement

of NiTi alloy by pre-strain warm surface mechanical attrition treatment, Acta Mater. 240 (2022) 118269.

[28] H. Lin, P. Hua, K. Huang, Q. Li, Q. Sun, Grain boundary and dislocation strengthening of nanocrystalline NiTi for stable elastocaloric cooling, Scr. Mater. 226 (2023) 115227.

[29] P. Hua, M. Xia, Y. Onuki, Q. Sun, Nanocomposite NiTi shape memory alloy with high strength and fatigue resistance, Nat. Nanotechnol. 16(4) (2021) 409-413.

[30] V. Brailovski, S. Prokoshkin, E. Bastarash, V. Demers, K.E. Inaekyan, I. Khmelevskaya, Thermal stability and nanocrystallization of amorphous Ti-Ni alloys prepared by cold rolling and post-deformation annealing, Mater. Sci. Forum 539-543 (2007) 1964-1970.

[31] Y. Zhu, X. Wu, Heterostructured materials, Prog. Mater. Sci. 131 (2023) 101019.

[32] J. Chen, H. Yin, Q. Sun, Effects of grain size on fatigue crack growth behaviors of nanocrystalline superelastic NiTi shape memory alloys, Acta Mater. 195 (2020) 141-150.

[33] H. Gu, L. Bumke, C. Chluba, E. Quandt, R.D. James, Phase engineering and supercompatibility of shape memory alloys, Mater. Today 21(3) (2018) 265-277.

[34] P. Sedmák, P. Šittner, J. Pilch, C. Curfs, Instability of cyclic superelastic deformation of NiTi investigated by synchrotron X-ray diffraction, Acta Mater. 94 (2015) 257-270.

[35] N. Nayan, D. Roy, V. Buravalla, U. Ramamurty, Unnotched fatigue behavior of an austenitic Ni–Ti shape memory alloy, Mater. Sci. Eng., A 497(1) (2008) 333-340.

[36] M. Fx Wagner, N. Nayan, U. Ramamurty, Healing of fatigue damage in NiTi shape memory alloys, J. Phys. D: Appl. Phys. 41(18) (2008) 185408.

[37] R. Delville, B. Malard, J. Pilch, P. Sittner, D. Schryvers, Transmission electron microscopy investigation of dislocation slip during superelastic cycling of Ni–Ti wires, Int. J. Plast. 27(2) (2011) 282-297.

[38] R. Delville, B. Malard, J. Pilch, P. Sittner, D. Schryvers, Microstructure changes during non-conventional heat treatment of thin Ni–Ti wires by pulsed electric current studied by transmission electron microscopy, Acta Mater. 58(13) (2010) 4503-4515.

[39] L. Bumke, C. Chluba, H. Ossmer, C. Zamponi, M. Kohl, E. Quandt, Cobalt gradient evolution in sputtered TiNiCuCo films for elastocaloric cooling, Phys. Status Solidi B 255(2) (2018) 1700299.

[40] C. Chluba, H. Ossmer, C. Zamponi, M. Kohl, E. Quandt, Ultra-low fatigue quaternary TiNi-based films for elastocaloric cooling, Shap. Mem. Superelasticity 2(1) (2016) 95-103.

[41] H. Ossmer, F. Lambrecht, M. Gültig, C. Chluba, E. Quandt, M. Kohl, Evolution of temperature profiles in TiNi films for elastocaloric cooling, Acta Mater. 81 (2014) 9-20.

[42] F. Bruederlin, L. Bumke, C. Chluba, H. Ossmer, E. Quandt, M. Kohl, Elastocaloric cooling on the miniature scale: A review on materials and device engineering, Energy Technol. 6(8) (2018) 1588-1604.

[43] M. Schmidt, A. Schütze, S. Seelecke, Scientific test setup for investigation of shape memory alloy based elastocaloric cooling processes, Int. J. Refrig. 54 (2015) 88-97.

[44] H. Wang, H. Huang, J. Xie, Effects of strain rate and measuring temperature on the elastocaloric cooling in a columnar-grained $Cu_{71}Al_{17.5}Mn_{11.5}$ shape memory alloy, Metals 7(12) (2017) 527.

[45] S. Qian, J. Ling, Y. Hwang, R. Radermacher, I. Takeuchi, Thermodynamics cycle analysis and numerical modeling of thermoelastic cooling systems, Int. J. Refrig. 56 (2015) 65-80.

[46] S. Qian, Y. Geng, Y. Wang, T.E. Pillsbury, Y. Hada, Y. Yamaguchi, K. Fujimoto, Y. Hwang, R. Radermacher, J. Cui, Y. Yuki, K. Toyotake, I. Takeuchi, Elastocaloric effect in CuAlZn and CuAlMn shape memory alloys under compression, Philos. Trans. R. Soc., A 374(2074) (2016) 20150309.

[47] H. Wang, H.-Y. Huang, Y.-J. Su, Tuning the operation temperature window of the elastocaloric effect in Cu–Al–Mn shape memory alloys by composition design, J. Alloys Compd. 828 (2020) 154265.

[48] A. Shen, D. Zhao, W. Sun, J. Liu, C. Li, Elastocaloric effect in a $Co_{50}Ni_{20}Ga_{30}$ single crystal, Scr. Mater. 127 (2017) 1-5.

[49] M.T. Khan, Y. Wang, C. Wang, X. Liao, S. Yang, X. Song, X. Ren, Combination of conventional elastocaloric and magnetocaloric effects in a $Co_{37}Ni_{35}Al_{28}$ ferromagnetic shape memory alloy, Scr. Mater. 146 (2018) 182-186.

[50] K. Liu, Y. Yuan, S. Ma, G. Feng, D. Wan, S. Wang, C. Chen, X. Luo, Z. Zhong, Large elastocaloric effect around room temperature in directionally solidified $Co_{49}Fe_3V_{33}Ga_{15}$ superelastic alloy, J. Alloys Compd. 884 (2021) 161094.

[51] F. Xiao, T. Fukuda, T. Kakeshita, Significant elastocaloric effect in a Fe-31.2Pd (at. %) single crystal, Appl. Phys. Lett. 102(16) (2013) 161914.

[52] Q. Shen, D. Zhao, W. Sun, Z. Wei, J. liu, Microstructure, martensitic transformation and elastocaloric effect in Pd-In-Fe polycrystalline shape memory alloys, Intermetallics 100 (2018) 27-31.

[53] Y. Li, D. Zhao, J. Liu, Giant and reversible room-temperature elastocaloric effect in a single-crystalline Ni-Fe-Ga magnetic shape memory alloy, Sci. Rep. 6 (2016) 25500.

[54] F. Xiao, M. Jin, J. Liu, X. Jin, Elastocaloric effect in $Ni_{50}Fe_{19}Ga_{27}Co_4$ single crystals, Acta Mater. 96 (2015) 292-300.

[55] Y. Xu, B. Lu, W. Sun, A. Yan, J. Liu, Large and reversible elastocaloric effect in dual-phase $Ni_{54}Fe_{19}Ga_{27}$ superelastic alloys, Appl. Phys. Lett. 106(20) (2015) 201903.

[56] Y. Shen, Z. Wei, W. Sun, Y. Zhang, E. Liu, J. Liu, Large elastocaloric effect in directionally solidified all-d-metal Heusler metamagnetic shape memory alloys, Acta Mater. 188 (2020) 677-685.

[57] L. Wei, X. Zhang, J. Liu, L. Geng, Orientation dependent cyclic stability of the elastocaloric effect in textured Ni-Mn-Ga alloys, AIP Adv. 8(5) (2018) 055312.

[58] Y. Li, W. Sun, D. Zhao, H. Xu, J. Liu, An 8 K elastocaloric temperature change induced by 1.3% transformation strain in $Ni_{44}Mn_{45-x}Sn_{11}Cu_x$ alloys, Scr. Mater. 130 (2017) 278-282.

[59] D. Zhao, J. Liu, X. Chen, W. Sun, Y. Li, M. Zhang, Y. Shao, H. Zhang, A. Yan, Giant caloric effect of low-hysteresis metamagnetic shape memory alloys with exceptional cyclic functionality, Acta Mater. 133 (2017) 217-223.

[60] Y.J. Huang, Q.D. Hu, N.M. Bruno, J.-H. Chen, I. Karaman, J.H. Ross, J.G. Li, Giant elastocaloric effect in directionally solidified Ni–Mn–In magnetic shape memory alloy, Scr. Mater. 105 (2015) 42-45.

[61] B. Lu, P. Zhang, Y. Xu, W. Sun, J. Liu, Elastocaloric effect in $Ni_{45}Mn_{36.4}In_{13.6}Co_5$ metamagnetic shape memory alloys under mechanical cycling, Mater. Lett. 148 (2015) 110-113.

[62] Z.Y. Wei, W. Sun, Q. Shen, Y. Shen, Y.F. Zhang, E.K. Liu, J. Liu, Elastocaloric effect of all-d-metal Heusler NiMnTi(Co) magnetic shape memory alloys by digital image correlation and infrared thermography, Appl. Phys. Lett. 114(10) (2019) 101903.

[63] D. Li, Z. Li, X. Zhang, B. Yang, D. Wang, X. Zhao, L. Zuo, Enhanced cyclability of elastocaloric effect in a directionally solidified $Ni_{55}Mn_{18}Ga_{26}Ti_1$ alloy with low hysteresis, Scr. Mater. 189 (2020) 78-83.

[64] J. Wang, Q. Yu, K. Xu, C. Zhang, Y. Wu, C. Jiang, Large room-temperature elastocaloric effect of $Ni_{57}Mn_{18}Ga_{21}In_4$ alloy undergoing a magnetostructural coupling transition, Scr. Mater. 130 (2017) 148-151.

[65] Z. Deng, K. Huang, H. Yin, Q. Sun, Temperature-dependent mechanical properties and elastocaloric

effects of multiphase nanocrystalline NiTi alloys, J. Alloys Compd. 938 (2023) 168547.

[66] L. Ding, Y. Zhou, Y. Xu, P. Dang, X. Ding, J. Sun, T. Lookman, D. Xue, Learning from superelasticity data to search for Ti-Ni alloys with large elastocaloric effect, Acta Mater. 218 (2021) 117200.

[67] H. Johra, Performance overview of caloric heat pumps: magnetocaloric, elastocaloric, electrocaloric and barocaloric systems, CLIMA 2022: REHVA 14th HVAC World Congress, Department of the Built Environment, Aalborg University, 2022.

[68] T.M. Correia, J.S. Young, R.W. Whatmore, J.F. Scott, N.D. Mathur, Q. Zhang, Investigation of the electrocaloric effect in a $PbMg_{2/3}Nb_{1/3}O_3$-$PbTiO_3$ relaxor thin film, Appl. Phys. Lett. 95(18) (2009) 182904.

[69] B. Neese, B. Chu, S.-G. Lu, Y. Wang, E. Furman, Q.M. Zhang, Large electrocaloric effect in ferroelectric polymers near room temperature, Science 321(5890) (2008) 821-823.

[70] E. Defay, S. Crossley, S. Kar-Narayan, X. Moya, N.D. Mathur, The electrocaloric efficiency of ceramic and polymer films, Adv. Mater. 25(24) (2013) 3337-3342.

[71] A.M.G. Carvalho, W. Imamura, E.O. Usuda, N.M. Bom, Giant room-temperature barocaloric effects in PDMS rubber at low pressures, Eur. Polym. J. 99 (2018) 212-221.

[72] E.O. Usuda, N.M. Bom, A.M.G. Carvalho, Large barocaloric effects at low pressures in natural rubber, Eur. Polym. J. 92 (2017) 287-293.

[73] N. Weerasekera, K. Ajjarapu, K. Sudan, G. Sumanasekera, K. Kate, B. Bhatia, Barocaloric Properties of Thermoplastic Elastomers, Front. Energy Res. (10) (2022) 573.

[74] E.D. X. Moya, V. Heine, N.D. Mathur, Too cool to work, Nat. Phys. 11 (2015) 202-205.

[75] M.P. Annaorazov, S.A. Nikitin, A.L. Tyurin, K.A. Asatryan, A.K. Dovletov, Anomalously high entropy change in FeRh alloy, J. Appl. Phys. 79(3) (1996) 1689-1695.

[76] T. Kihara, X. Xu, W. Ito, R. Kainuma, M. Tokunaga, Direct measurements of inverse magnetocaloric effects in metamagnetic shape-memory alloy NiCoMnIn, Phys. Rev. B 90(21) (2014) 214409.

[77] L. Bumke, C. Zamponi, J. Jetter, E. Quandt, Cu-rich $Ti_{52.8}Ni_{22.2}Cu_{22.5}Co_{2.5}$ shape memory alloy films with ultra-low fatigue for elastocaloric applications, J. Appl. Phys. 127(22) (2020) 225105.

[78] X. Tang, Y. Feng, H. Wang, P. Wang, Enhanced elastocaloric effect and cycle stability in B and Cu co-doping Ni-Mn-In polycrystals, Appl. Phys. Lett. 114(3) (2019) 033901.

[79] X. Wu, P. Jiang, L. Chen, F. Yuan, Y.T. Zhu, Extraordinary strain hardening by gradient structure, Proc. Natl. Acad. Sci. U. S. A. 111(20) (2014) 7197-7201.

[80] S.L. Semiatin, H.R. Piehler, Deformation of sandwich sheet materials in uniaxial tension, Metall. Trans. A 10(1) (1979) 85-96.

[81] K. Otsuka, X. Ren, Physical metallurgy of Ti–Ni-based shape memory alloys, Prog. Mater. Sci. 50(5) (2005) 511-678.